Temperature damping of magneto-intersubband resistance oscillations in magnetically entangled subbands

Sara Abedi and Sergey Vitkalov [*]

Physics Department, City College of the City University of New York, New York 10031, USA

A. A. Bykov and A. K. Bakarov

Rzhanov Institute of Semiconductor Physics, Siberian Branch, Russian Academy of Sciences, Novosibirsk 630090, Russia

Magneto-intersubband resistance oscillations (MISOs) of highly mobile 2D electrons in symmetric GaAs quantum wells with two populated subbands are studied in magnetic fields tilted from the normal to the 2D electron layer at different temperatures T. A decrease of MISO amplitude with temperature increase is observed. At moderate tilts, the temperature decrease of MISO amplitude is consistent with a decrease of the Dingle factor due to a reduction of the quantum electron lifetime at high temperatures. At large tilts, a different regime of strong MISO suppression with the temperature is observed. The proposed model relates this suppression to magnetic entanglement between subbands, leading to beating in oscillating density of states. The model yields corresponding temperature damping factor: $A_{\mathrm{MISO}}(T) = X/\sinh(X)$, where $X = 2\pi^2 kT \delta f$ and δf is the difference frequency of oscillations of density of states in two subbands. This factor is in agreement with experiments. A Fermi liquid enhancement of MISO amplitude is observed.

I. INTRODUCTION

The orbital quantization of electron trajectories and spectrum in magnetic fields significantly affects the electron transport in condensed materials [1–3]. Shubnikov-de Haas (SdH) resistance oscillations [1] and quantum Hall effect (QHE) [4] are remarkable effects of the orbital quantization. These effects occur at a temperature, T, which is less than the cyclotron energy, $\Delta_c = \hbar\omega_c$, separating Landau levels. Here ω_c is the cyclotron frequency. At high temperatures, $kT > \hbar\omega_c$, both SdH oscillations and QHE are absent due to a spectral averaging of the oscillating density of states (DOS) in the energy interval, $\delta\epsilon \approx kT$, in a vicinity of Fermi energy, ϵ_F.

At high temperatures, $kT > \hbar\omega_c$, electron systems with multiple populated subbands continue to exhibit quantum resistance oscillations [5–10]. These magneto-intersubband oscillations (MISOs) of the resistance are due to an alignment between Landau levels from different subbands i and j with corresponding energies E_i and E_j at the bottom of the subbands. Resistance maxima occur at magnetic fields in which the gap between the bottoms of the subbands, $\Delta_{ij} = E_i - E_j$, is a multiple of the Landau level spacing: $\Delta_{ij} = k\hbar\omega_c$, where k is an integer [11–15]. At this condition, Landau levels of two subbands overlap and the electron elastic scattering on impurities is enhanced due to the possibility of electron transitions between the overlapped quantum levels of ith and jth subbands. At magnetic fields corresponding to the condition $\Delta_{ij} = (k + 1/2)\hbar\omega_c$, the intersubband electron scattering is

suppressed since the quantum levels of two subbands are misaligned. The spectral overlap between two subbands oscillates with the magnetic field and leads to MISOs, which are periodic in the inverse magnetic field.

Recently, we studied transport properties of high quality GaAs quantum wells with two populated subbands in tilted magnetic fields [16]. The goals of that study were to detect effects of the spin (Zeeman) splitting on MISOs, as well as to investigate the effect of the spin splitting on quantum positive magnetoresistance (QPMR) [17–20] in a 2D system with two populated subbands. These experiments have demonstrated a significant reduction of the QPMR with the application of the in-plane magnetic field, which was in good agreement with the modification of the electron spectrum via Zeeman effect with g factor $g \approx 0.43 \pm 0.07$. MISOs also have a strong reduction of the magnitude with the in-plane magnetic field. However, in contrast to the QPMR, the MISO reduction is found to be predominantly related to a modification of the electron spectrum via a magnetic entanglement of two subbands, induced by the in-plane magnetic field [16].

In zero magnetic field, the electron motion in a quantum well can be separated on two independent parts: the lateral motion along the 2D layer and the vertical motion (perpendicular to 2D layer), which is quantized. In a perpendicular magnetic field, the lateral motion is also quantized, forming Landau levels, but the lateral and vertical motions are still separable. The eigenstates of the systems can be, therefore, represented as a product of two wave functions, corresponding to two eigenstates for vertical and lateral motions. The in-plane magnetic field couples vertical and lateral electron motions, making these electron motions to be nonseparable or entangled. As a result, in a tilted magnetic field, the

[*]Corresponding author: svitkalov@ccny.cuny.edu

eigenstates of the system cannot be presented as a product of two wave functions, corresponding to lateral and vertical motions but are presented as a linear superposition of such products. In this paper, we call this effect magnetic entanglement of two subbands since mathematically the effect is similar to the quantum entanglement of particles in many-body physics.

It is important to mention that the Hamiltonian Eq. (2), describing the entangled subbands, appears in QED models, where a photon mode/harmonic oscillator, represented in our case by Landau levels, couples to a qubit, represented by two subbands. Such systems have been used in atomic physics [21] and quantum optics as well as with superconducting circuits [22,23]. Recently, this model was exploited for 2D electrons on the surface of liquid He-4 [24].

In this paper, the temperature dependence of MISO amplitude is studied in a broad range of angles θ between the magnetic field, **B**, and the normal to the 2D layer. At small angles, the MISO temperature dependence is controlled by temperature variations of the electron quantum lifetime entering the Dingle factor. At large angles θ, a different regime of the temperature damping of MISO is observed, demonstrating an exponentially strong decrease of MISO magnitude with the temperature. The proposed model relates the observed MISO suppression with the magnetic entanglement of subbands leading to the MISO damping factor: $A_{\mathrm{MISO}}(T) = X/\sinh(X)$, where $X = 2\pi^2 kT \delta f$ and δf is the difference frequency of oscillations of the DOS in two subbands. A comparison with the model reveals an enhancement of MISO magnitude, which has a Fermi liquid origin.

The paper has the following organization. Section II presents details of the experimental setup. Experimental results are presented in Sec. III. In Sec. IV, the model leading to MISO is discussed in detail. Section V presents a comparison and discussion of the experimental results and model outcomes. Appendix A presents cyclotron mass calculations and computations of the parameter X for magnetically entangled subbands. Appendix B contain details of the derivation of Eq. (10).

II. EXPERIMENTAL SETUP

Studied GaAs quantum wells were grown by molecular beam epitaxy on a semi-insulating (001) GaAs substrate. The material was fabricated from a selectively doped GaAs single quantum well of width $d = 26$ nm sandwiched between AlAs/GaAs superlattice screening barriers [25–29]. The studied samples were etched in the shape of a Hall bar. The width and the length of the measured part of the samples are $W = 50\,\mu$m and $L = 250\,\mu$m. AuGe eutectic was used to provide electric contacts to the 2D electron gas. Samples were studied at different temperatures, from 5.5 Kelvin to 12.5 Kelvin in magnetic fields up to 7 Tesla applied at different angles θ relative to the normal to 2D layers and perpendicular to the applied current. The angle θ is evaluated using Hall voltage $V_H = B_\perp/(en_T)$, which is proportional to the perpendicular component, $B_\perp = B \cdot \cos(\theta)$, of the total magnetic field **B**.

The total electron density of sample S1, $n_T = (8.0 \pm 0.03) \times 10^{11} \mathrm{cm}^{-2}$, was evaluated from the Hall measurements taken in classically strong magnetic fields [2]. An
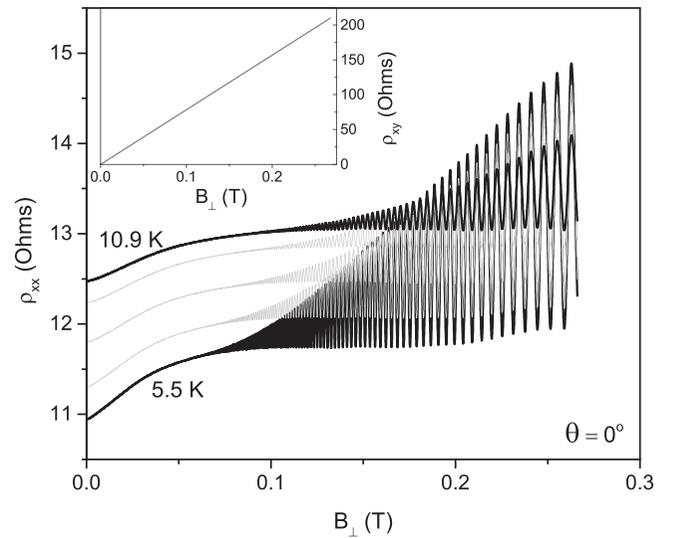
FIG. 1. Dependencies of the dissipative resistivity of 2D electrons, ρ_{xx}, on perpendicular magnetic field taken at different temperatures: from bottom to top $T = 5.5, 6.9, 8.5, 10.1,$ and 10.9 K. The inset shows the Hall resistivity, ρ_{xy}, in a perpendicular magnetic field at the same set of temperatures as in the main plot. Angle $\theta = 0^\circ$.

average electron mobility $\mu \approx 72\,\mathrm{m}^2/Vs$ was obtained from n_T and the zero-field resistivity. An analysis of the periodicity of MISOs in the inverse magnetic field yields the gap $\Delta_{12} = 15.15$ meV between the bottoms of the conducting subbands, Fermi energy $E_F = 21.83$ meV and electron densities $n_1 = 6.12 \times 10^{11} \mathrm{cm}^{-2}$ and $n_2 = 1.87 \times 10^{11} \mathrm{cm}^{-2}$ in the two populated subbands. Sample S2 has density $n_T \approx 8.0 \times 10^{11} \mathrm{cm}^{-2}$, mobility $\mu \approx 100 \times \mathrm{m}^2/\mathrm{Vs}$ and the gap $\Delta_{12} = 15.10$ meV. Both samples have demonstrated similar behaviors in magnetic fields. Below we present data for sample S1.

Sample resistance was measured using the four-point probe method. We applied a 133 Hz *ac* excitation $I_{\mathrm{ac}} = 1\,\mu$A through the current contacts and measured the longitudinal (in the direction of the electric current, *x* direction) and Hall ac (along *y* direction) voltages (V_{xx}^{ac} and V_H^{ac}) using two lock-in amplifiers with $10\,\mathrm{M\Omega}$ input impedance. The measurements were done in the linear regime in which the voltages are proportional to the applied current.

III. EXPERIMENTAL RESULTS

Figure 1 shows dependencies of the dissipative resistivity of 2D electrons on the perpendicular magnetic field $B_\perp$, taken at different temperatures T and the angle $\theta = 0^\circ$ between the direction of the magnetic field **B** and the normal to the 2D layer. At $\theta = 0^\circ$, two subbands are disentangled. At $T = 5.5$ K and small magnetic field ($B_\perp < 0.05$ T), the curve demonstrates an increase related to classical magnetoresistivity [2,16]. At higher magnetic fields, $B_\perp > 0.08$ T, the resistivity starts to oscillate with progressively larger magnitude at higher field. These oscillations are MISO. MISO maxima correspond to the condition

$$\Delta_{12} = k\hbar\omega_c, \tag{1}$$
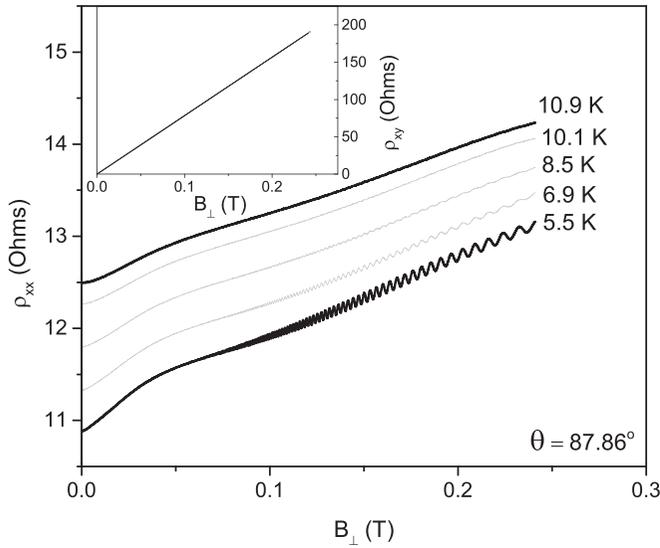
FIG. 2. Dependencies of the dissipative resistivity of 2D electrons, ρ_{xx}, on perpendicular magnetic field taken at different temperatures: from bottom to top: $T = 5.5$, 6.9, 8.5, 10.1, and 10.9 K. The inset shows the Hall resistivity, ρ_{xy}, in a perpendicular magnetic field at the same set of temperatures as in the main plot. Angle $\theta = 87.86°$.

FIG. 3. Oscillating content of magnetoresistivity ρ_{xx} at two different temperatures as labeled. (a) disentangled subbands at angle $\theta = 0°$, (b) entangled subbands at angle $\theta = 87.05°$.

where $\Delta_{12} = E_2 - E_1$ is the energy difference between bottoms of two occupied subbands and the index k is a positive integer [13,15].

The temperature significantly affects the MISO magnitude. At temperature 10.9 K, the MISO magnitude is substantially smaller the one at $T = 5.5$ K. Furthermore at a higher temperature the oscillations starts at a higher magnetic field. Both effects are a result of an increase of the quantum scattering rate of electrons at higher temperature due to the enhancement of electron-electron scattering [8,9,19]. This rate enters the Dingle factor, affecting strongly MISO magnitude [see below Eq. (10)]. The inset to Fig. 1 shows the Hall resistivity at different temperatures. The inset indicates that the Hall resistivity and thus the total electron density in the system are not affected by temperature.

Figure 2 shows dependencies of the dissipative resistivity of 2D electrons on the perpendicular magnetic field $B_\perp$, taken at different temperatures T but at the angle $\theta = 87.86$ °. At $\theta = 87.86°$, two subbands are entangled by the in-plane magnetic field. At $T = 5.5$ K and small magnetic field ($B_\perp <$ 0.05 T), the curve continues to demonstrate an increase related to classical magnetoresistivity [2,16]. At higher magnetic fields, $B_\perp > 0.08$ T, the resistivity starts to oscillate but with a magnitude which is significantly smaller than the one shown in Fig. 1 for disentangled subbands. The inset to the figure indicates that the Hall resistivity and the total electron density, n_T, are still temperature independent and stays the same for disentangled subbands.

To facilitate the analysis of the oscillating content, the monotonic background ρ_{xx}^b, obtained by an averaging of the oscillations in reciprocal perpendicular magnetic fields, is removed from the magnetoresistivity $\rho_{xx}(B_\perp)$. Figure 3 presents the remaining oscillating content of the magnetoresistivity, ρ_{MISO}, as a function of the reciprocal perpendicular magnetic
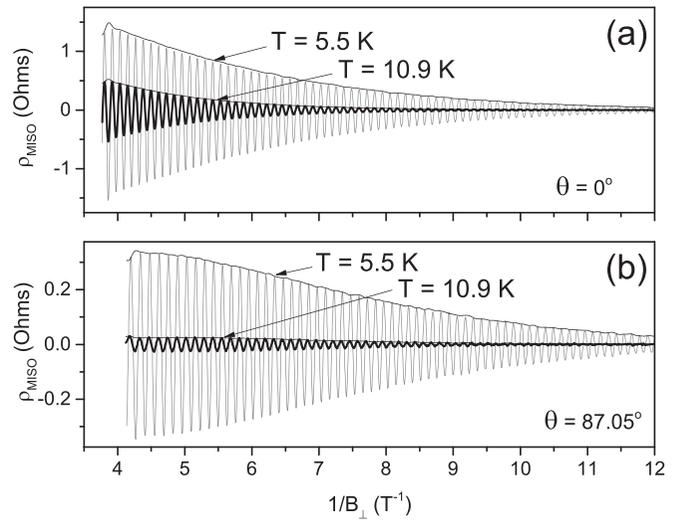
field $B_\perp^{-1}$ for two temperatures as labeled. The thin solid lines indicate envelopes of the oscillating content used in the analysis below.

For disentangled subbands, Fig. 3(a) demonstrates that at the high temperature $T = 10.9$ K, the MISO magnitude is smaller than the one at $T = 5.5$ K. An analysis of the MISO envelope indicates that the MISO magnitude decreases exponentially with $1/B_\perp$ at a small $1/B_\perp$. The rate of the exponential decrease is stronger at the higher temperature. Both the thermal suppression of MISO and the enhancement of the MISO reduction with $1/B_\perp$ result from the increase of the quantum scattering rate of 2D electrons, $1/\tau_q$, due to the increase of electron-electron scattering at high temperatures.

Figure 3(b) demonstrates the dependence of MISO on $1/B_\perp$ for the magnetically entangled subbands at $\theta = 87.05°$. The decrease of MISO magnitude with $1/B_\perp$ is different from the exponential decrease of the disentangled subbands. The magnetic field dependence tends to saturate at small $1/B_\perp$ in contrast to the one shown in Fig. 3(a). For the entangled subbands, the MISO magnitude is significantly reduced. Furthermore, a rough analysis indicates that the relative decrease of the MISO magnitude with the temperature is substantially stronger than the one for disentangled subbands. In particular, at $1/B_\perp = 5$ (1/T) for the disentangled subbands, the ratio between MISO magnitudes at $T_1 = 5.5$ K and $T_2 = 10.9$ K is close to 3, while for the entangled subbands the ratio is larger and close to 10.

Figure 4 presents an evolution of the temperature dependence of the MISO magnitude with the angle θ at fixed $1/B_\perp = 5$ (1/T). Figure 4(a) shows the dependence of the normalized MISO magnitude on T^2. At a small subband entanglement ($\theta = 0°$ and 84.59°), the MISO magnitude drops exponentially with T^2 in good agreement with the solid straight line presenting the T^2 exponential decrease at $\theta = 0°$. At larger angles ($\theta = 87.05°$ and 87.86°), the MISO drop becomes stronger and deviates from the T^2 dependence.
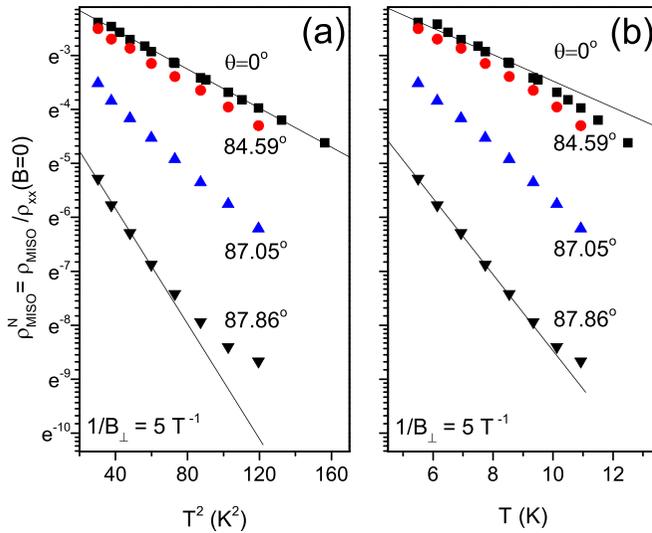
FIG. 4. Temperature dependence of normalized amplitude of MISO, $\rho_{\mathrm{MISO}}^{N} = \rho_{\mathrm{MISO}}/\rho_{xx}(\mathbf{B} = 0)$ at $B_{\perp}^{-1} = 5$ (1/T). (a) The dependence is plotted versus T^2, (b) the dependence is plotted versus T.

In Fig. 4(b), the symbols present the dependence of normalized MISO amplitude on temperature T. The solid straight lines demonstrate the exponential decrease with T. At small subband entanglement ($\theta = 0$; 84.59°), the MISO magnitude does not decrease exponentially with T. The dependence deviates considerably from the solid straight line. In contrast, at the largest angle (87.86°), the MISO reduction is consistent with the exponential decrease with T and follows the solid straight line. Thus, Fig. 4 shows that the decrease of MISO amplitude with temperature is qualitatively different for the entangled subbands, indicating a different mechanism leading to the MISO damping. This regime of thermal MISO damping is analyzed below within a model, taking into account the magnetic entanglement of 2D subbands.

IV. MODEL OF QUANTUM ELECTRON TRANSPORT

In perpendicular magnetic fields (at $\theta = 0°$), a microscopic theory of MISO is presented in Refs. [13–15]. In this theory, the electron spectra of two subbands evolve in magnetic fields quite independently. The reason is that at $\theta = 0°$, the lateral (in the 2D layer) and vertical (perpendicular to the layer) electron motions are separable and do not affect each other. In a tilted magnetic field, there is a component of the field, $B_{\parallel}$, which is parallel to the 2D conducting layer. This parallel component couples the lateral and vertical electron motions and electron spectra of two subbands become magnetically entangled. A MISO model, which takes into account this magnetic entanglement between two subbands, has been proposed recently. The model demonstrates a significant decrease of MISO amplitude with the magnetic field tilt [16]. A comparison with corresponding experiments indicates that the magnetic entanglement between subbands is the dominant mechanism leading to the angular decrease of the MISO amplitude in GaAs quantum wells. Zeeman spin splitting is found to provide a subleading contribution to the effect [16].

Below, this model is used to analyze the temperature dependence of the MISO amplitude in tilted magnetic fields. The Zeeman effect is ignored. The analysis reveals a *universal* temperature-dependent factor which controls the MISO amplitude in magnetically entangled subbands. The amplitude reduction is found to be exponential with the temperature in the regime of a strong magnetic entanglement. In many respects, the physics of this additional temperature factor is similar to the one for SdH oscillations. The obtained factor describes a general MISO property.

A. Spectrum in tilted magnetic field

Let 2D electrons propagate along the xy plane and the z axes perpendicular to the plane. In quantum wells, the spatial subbands are the result of quantization of the electron wave function in the z direction. Index $i = 1(2)$ labels the low (high) subband with the energy $E_1(E_2)$ at the bottom of the subband. The subband separation is $\Delta_{12} = E_2 - E_1$.

With no in-plane magnetic field applied, the spatial subbands are coupled to each other via elastic scattering. An in-plane magnetic field, $B_{\parallel}$, provides an additional coupling via Lorentz force coming from the last term of the Hamiltonian H presented by Eq. (2). This additional $B_{\parallel}$ coupling preserves the degeneracy of the quantum levels but induces variations of the electron spectrum, which, due to the relativistic origin of the Lorentz force, are dependent on the energy (velocity). These spectrum variations destroy the complete spectral overlap between Landau levels from different subbands, existing at zero in-plane magnetic field. This leads to the angular decrease of the MISO amplitude [16]. Below, we investigate how this decrease depends on the temperature following to the developed approach [16].

To estimate the effect, the electron spectrum of an ideal two subband system without impurity scattering is computed numerically in a tilted magnetic field. The impurity scattering is then introduced by a broadening of the bare quantum levels using a Gaussian shape of the DOS with the preserved level degeneracy.

We consider a quantum well of a width d in the z direction formed by a rectangular electrostatic potential $V(z)$ with infinitely high walls and placed in a tilted magnetic field $\mathbf{B} = (-B_{\parallel}, 0, B_{\perp})$. Electrons are described by the Hamiltonian [16],

$$H = \frac{\hbar^2 k_x^2}{2m_0} + \frac{e^2 B_{\perp}^2}{2m_0}x^2 + \frac{\hbar^2 k_z^2}{2m_0} + V(z) + \frac{e^2 B_{\parallel}^2}{2m_0}z^2$$
$$+ \frac{e^2 B_{\perp} B_{\parallel}}{m_0}xz, \qquad (2)$$

where m_0 is electron band mass. To obtain Eq. (2), we have used the gauge $(0, B_{\perp}x + B_{\parallel}z, 0)$ of the vector potential and applied the transformation $x \rightarrow x - \hbar k_y/eB_{\perp}$.

The first four terms of the Hamiltonian describe the 2D electron system in a perpendicular magnetic field. The corresponding eigenfunctions of the system are $|N, \xi\rangle$, where $N = 0, 1, 2...$ presents the Nth Landau level (the lateral quantization) and $\xi = S, AS$ describes the symmetric (S) and antisymmetric (AS) configurations of the wave function in the z direction

(vertical quantization): $|N, S\rangle = |N\rangle (2/d)^{1/2} \cos(\pi z/d)$ and $|N, AS\rangle = |N\rangle (2/d)^{1/2} \sin(2\pi z/d)$.

Using functions $|N, \xi\rangle$ as the basis set, one can present the Hamiltonian in matrix form. The matrix contains four matrix blocks: $\hat{H} = (\hat{E}^S, \hat{T}; \hat{T}, \hat{E}^{AS})$, where the semicolon separates rows. The diagonal matrices, $\hat{E}^S$ and $\hat{E}^{AS}$, represent energy of the symmetric and antisymmetric wave functions in different orbital states N:

$$E_{mn}^S = \delta_{mn}\left[\hbar\omega_c\left((n-1) + \frac{1}{2}\right) + \frac{e^2 B_\parallel^2 d^2[\frac{1}{12} - \frac{1}{2\pi^2}]}{2m_0}\right],$$

$$E_{mn}^{AS} = \delta_{mn}\left[\hbar\omega_c\left((n-1) + \frac{1}{2}\right) + \Delta_{12} + \frac{e^2 B_\parallel^2 d^2[\frac{1}{12} - \frac{1}{8\pi^2}]}{2m_0}\right], \quad (3)$$

where $\Delta_{12} = E_2 - E_1$ is the energy difference between the bottoms of two spatial subbands and indexes $m = 1, 2 \ldots N_{\max}$ and $n = 1, 2 \ldots N_{\max}$ numerate rows and columns of the matrix, correspondingly. These indexes are related to the orbital number N: $n, m = N + 1$, since the orbital number $N = 0, 1, 2 \ldots$ In numerical computations, the maximum number $N_{\max}$ is chosen to be about twice larger than the orbital number N_F corresponding to Fermi energy ϵ_F. Further increase of $N_{\max}$ shows a very small (within 1%) deviation from the dependencies obtained at $N_{\max} \approx 2N_F$. This also indicates that the contributions of the third and higher spatial subbands with a higher energy can be ignored in the spectrum computation. It supports the two subband approximation used in the paper.

The first term in Eq. (3) describes the orbital quantization of electron motion. The last term in Eq. (3) describes the diamagnetic shift of the quantum levels and relates to the fifth term in Eq. (2). In the basis set $|N, \xi\rangle$, the diamagnetic term is proportional to $\langle\xi|z^2|\xi\rangle$. The diamagnetic terms do not depend on N. The diamagnetic terms lead to an increase of the gap, E_g, between bottoms of subbands with the in-plane magnetic field:

$$E_g(B_\parallel) = \Delta_{12} + \frac{3}{16\pi^2}\frac{e^2 B_\parallel^2 d^2}{m_0}. \quad (4)$$

The off-diagonal matrix $\hat{T}$ is related to the last term in Eq. (2). This matrix mixes symmetric and antisymmetric states. Since $x = l_{B\perp}(a^* + a)/\sqrt{2}$ works as the raising a^* and lowering a operators of the Landau orbits, the last term in Eq. (2) couples Landau levels with orbital numbers different by one. Here $l_{B\perp} = (\hbar/eB_\perp)^{1/2}$ is the magnetic length in $B_\perp$. As a result, for $n > m$, the matrix element T_{mn} between states $|N, S\rangle$ and $|N + 1, AS\rangle$ is

$$T_{mn} = \delta_{m+1,n}\frac{e^2 B_\parallel B_\perp l_{B\perp}}{m_0}\langle N|\frac{a^* + a}{\sqrt{2}}|N + 1\rangle\langle S|z|AS\rangle$$

$$= \delta_{m+1,n}\hbar\omega_c\left[\frac{16 B_\parallel d}{9\pi^2 B_\perp l_{B\perp}}\right](n/2)^{1/2}. \quad (5)$$

The matrix $\hat{T}$ is a symmetric matrix: $T_{mn} = T_{nm}$.

The Hamiltonian $\hat{H}$ is diagonalized numerically at different magnetic fields $B_\perp$ and $B_\parallel$. To analyze the spectrum, the obtained eigenvalues of the Hamiltonian are numerated in ascending order using positive integer index $l = 1, 2 \ldots$, which is named below as the Landau level index.
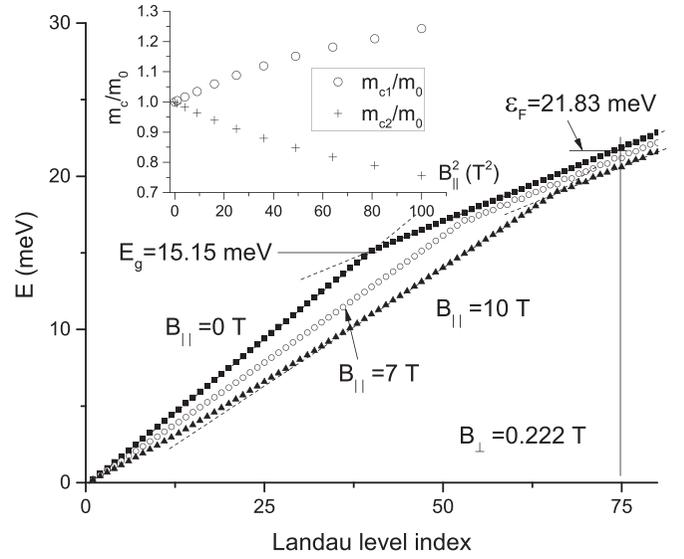
FIG. 5. Dependence of the energy of Landau levels, counted from the bottom of the lowest subband in GaAs quantum well of width $d = 27$ nm, on Landau level index, l, at different in-plane magnetic fields as labeled. Each symbol corresponds to a Landau level. Kinks in the dependencies occur at the energy corresponding to the bottom of the second subband, E_g. Decrease of the slope of the dependencies at $\epsilon < E_g$ with $B_\parallel$ indicates increase of the cyclotron mass m_{c1} in the first subband. The independence of the slope on $B_\parallel$ at $\epsilon > E_g$ suggests decrease of the mass m_{c2} in the second subband with $B_\parallel$. Vertical line at $l = 75$ marks the last populated Landau level in the studied system. $B_\perp = 0.222$ T. Inset shows divergence of cyclotron masses in two subbands with the in-plane magnetic field.

Figure 5 presents a dependence of the Landau-level energy, counted from the bottom of the first subband, on index l for different parallel magnetic fields as labeled. In the figure, each symbol corresponds to a Landau level. At $B_\parallel = 0$ T and $\epsilon < E_g = \Delta_{12}$, the quantum levels correspond to the first subband. These levels are evenly separated by the cyclotron energy $\Delta_c = \hbar\omega_c$, forming a straight line. The slope of this line is inversely proportional to the electron mass, m_0, since $\Delta_c \sim 1/m_0$. The slope is also inversely proportional to the DOS since DOS $\sim m_0$ for 2D parabolic bands. At $\epsilon > E_g$, the slope of the straight line is abruptly reduced by a factor of 2. This results from the contribution of the second subband to the total density of states, which starts at $\epsilon > E_g$. Since the mass in the second subband, m_0, is the same, the total DOS is doubled and the slope is reduced by factor of 2. The transition between these two straight lines occurs at $\epsilon = E_g$ and corresponds to the energy of the bottom of the second subband E_2.

At $B_\parallel = 7$ T and $\epsilon < \Delta_{12}$, the electron spectrum is different. At the same index l, the Landau levels of the first subband have a lower energy indicating an *increase* of the cyclotron mass in the subband: $m_{c1} > m_0$. This is the effect of the entanglement between subbands, induced by the in-plane magnetic field: the eigenstate Ψ_l of electron performing a cyclotron motion in the tilted magnetic field is now a linear superposition of the symmetric $|N, S\rangle$ and antisymmetric states $|N + n, AS\rangle$ of the Hamiltonian [Eq. (2)] at $B_\parallel = 0$ T. Although at $B_\parallel = 7$ T the open symbols form an apparent straight line, an

analysis indicates deviations of the data from the linear dependence, revealing a nonparabolicity of the spectrum. To simplify the presentation, we neglect these deviations and approximate the spectrum by a straight line. In other words, we consider the spectrum to be parabolic. Similar to the spectrum at $B_\parallel = 0$ T, the straight line changes its slope due to the contribution of the second subband to the DOS. The slope change occurs at a higher energy, E_g: $E_g > \Delta_{12}$ due to contribution of the diamagnetic terms to the gap [see Eq. (4)]. Within accuracy of 1%, the changed slope coincides with the slope obtained at $B_\parallel = 0$ T at $\epsilon > \Delta_{12}$. This indicates that at $\epsilon > E_g$, the total density of states is preserved and, therefore, the effective mass in the second subband is reduced by the in-plane field $B_\parallel$: $m_{c2} < m_0$, since $m_{c1} + m_{c2} = 2m_0 \sim$ total DOS at high energies. Progressively stronger variations of the masses are seen at higher in-plane field $B_\parallel = 10$ T.

The inset to the figure shows relative variations of the cyclotron masses in the two subbands induced by the in-plane magnetic field. The inset demonstrates that at small in-plane magnetic fields, the mass divergence is proportional to the square of the field. An analysis of the two-subband model in a small in-plane magnetic field, given in Appendix A, provides further support to the presented interpretation of the electron spectra.

The inset in Fig. 2 presents the Hall resistance taken at large tilt: $\theta = 86.87°$. The data indicates that the Hall coefficient, $R_H = 1/en_T$, which is the slope of the shown line, does not depend on the in-plane magnetic field. This suggests that the total density $n_T = n_1 + n_2$ and, thus, the electron population of Landau levels at fixed $B_\perp$: $l_p \approx n_T/n_0$ do not depend on $B_\parallel$. Here $n_0 = eB_\perp/(\pi\hbar)$ is the degeneracy of the Landau level (including the spin degeneracy) and l_p is the index of the highest populated level. In Fig. 5, the vertical line at $l = 75$ marks the highest populated Landau level at $B_\perp = 0.222$ T in the studied sample. At a fixed electron density (electron population), the increase of the electron mass m_{c1} drives the Fermi energy, E_F, down, while the increase of the energy gap E_g between the subbands moves the Fermi energy up. An interplay between these two effects results in a weak decrease of the Fermi energy with the in-plane magnetic field in the studied system.

The presented analysis above indicates that in tilted magnetic fields, the cyclotron masses in two subbands are different: $m_{c1} > m_{c2}$. Different cyclotron masses lead to different frequencies of the DOS oscillations induced by the orbital quantization in the energy space. Namely, in the first subband the DOS $\nu_1(\epsilon)$ oscillates at frequency $f_1 = 1/\hbar\omega_{c1} \sim m_{c1}$, while in the second subband, the DOS, $\nu_2(\epsilon)$ oscillates at frequency $f_2 = 1/\hbar\omega_{c2} \sim m_{c2}$, where ω_{ci} is the cyclotron frequency in ith subband. Thus, at the same $B_\perp$, the frequency f_1 is higher than f_2 since $m_{c1} > m_{c2}$. The difference between frequencies results in a beating of the total DOS oscillations in the energy space as shown in Fig. 6.

Figure 6 demonstrates the total DOS in a vicinity of Fermi energy: $\delta\epsilon = \epsilon - \epsilon_F$ at fixed perpendicular magnetic field $B_\perp = 0.244$ T and different in-plane magnetic field $B_\parallel$ as labeled. The DOS is evaluated via numerical diagonalization of Hamiltonian Eq. (2) and consecutive broadening of the Landau levels. To demonstrate the DOS beating clearly, we use the same quantum scattering time for both subbands
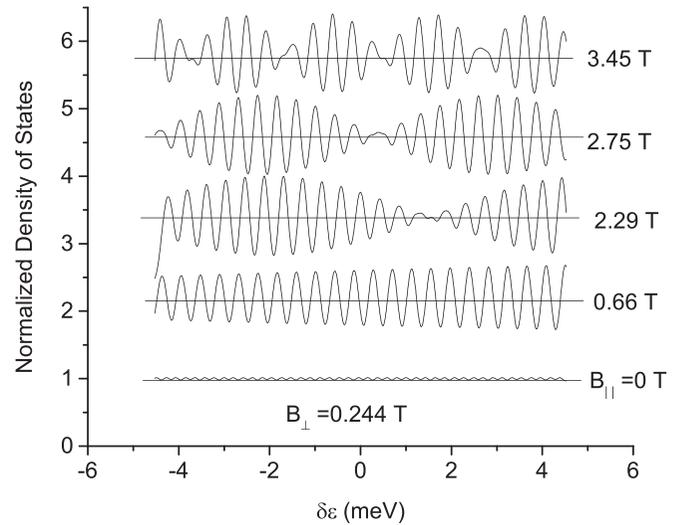
FIG. 6. Energy dependence of the normalized density of states in the vicinity of Fermi energy: $\delta\epsilon = \epsilon - \epsilon_F$ in quantum well of width $d = 33$ nm with two populated subbands, placed in perpendicular magnetic field $B_\perp = 0.244$ T and in-plane magnetic fields $B_\parallel$ as labeled. At $B_\parallel > 0$, the dependencies, shifted up for clarity, demonstrate beating pattern. The beating is related to the cyclotron mass divergence presented in the inset to Fig. 5. Quantum scattering time $\tau_q^{(1)} = \tau_q^{(2)} = 4$ ps.

$\tau_q^{(1)} = \tau_q^{(2)} = 4$ ps. The obtained DOS oscillations are well described by an interference of two cosine functions. At $B_\parallel = 0$ T, the DOS oscillations are significantly suppressed. This suppression is due to a destructive interference of the DOS oscillations in two subbands oscillating in the antiphase. This π phase shift between the DOS oscillations leads to a MISO minimum, while two in-phase DOS oscillations should interfere constructively and lead to a MISO maximum (not shown). A noticeable property of the pattern is that the destructive interference at $B_\parallel = 0$ T does not depend on the energy. This property is tightly related to the fact that the DOS oscillates at the same frequency $f = 1/\hbar\omega_c$ in both subbands at $B_\parallel = 0$ T.

The DOS oscillations at $B_\parallel = 0.66$ T present an example of a partially constructive interference. A noticeable property of these oscillations is an increase of the amplitude of the oscillations with the energy. This property is due to the fact that, in contrast to the DOS interference at $B_\parallel = 0$ T, the frequencies of two DOS oscillations at $B_\parallel = 0.66$ T are different: $f_1 > f_2$. Thus, the interference pattern between these oscillations depends on the energy, exhibiting the beating. The DOS oscillations at $B_\parallel = 2.29$, 2.75, and 3.45 T demonstrate the beating pattern with progressively shorter beating periods. The decrease of the beating period or increase of the beating frequency, f_b, is related to the increase of the difference frequency $\delta f = f_1 - f_2 = 2f_b$ with $B_\parallel$. This increase is due to the mass divergence, shown in the inset to Fig. 5, since $f_i \sim m_i$.

Below we explain qualitatively why the DOS beating leads to a temperature damping of MISOs. A more detailed consideration is given in the next section. The electron conductivity is determined by electrons in the kT vicinity of the Fermi energy ϵ_F [2]. The MISO amplitude is determined by the square

of the amplitude of the DOS oscillations averaged within the kT interval [13,15]. Let's assume that the energy interval kT is much less than the beating period ($\sim 1/\delta f$): $kT\delta f \ll 1$. At this condition, the MISO minimum (maximum) occurs when a node (antinode) of the beating pattern is located in the kT vicinity of ϵ_F, since at the node (antinode), the DOS oscillations have a small (large) magnitude. At large temperatures $kT\delta f \gg 1$, the kT interval contains both node (s) and antinode (s) and the averaged square of the DOS oscillations does not depend on the particular location of the beating pattern with respect to ϵ_F. At this condition, MISO oscillations should be suppressed. This consideration advocates for a decrease of the MISO amplitude with the temperature in magnetically entangled subbands.

B. Temperature damping of MISO in magnetically entangled subbands

We consider a 2D electron system with two populated parabolic subbands placed in a small quantizing perpendicular magnetic field $B_\perp$ and an in-plane magnetic field $B_\parallel$: $\mathbf{B} = (B_\perp, B_\parallel)$. In accordance with the presented numerical analysis of the electron spectrum (see also Appendix A) at nonzero $B_\parallel$ the cyclotron masses, $m_{c1} > m_{c2}$ and frequencies, $\omega_{c1} < \omega_{c2}$, are different. This difference leads to the DOS oscillating at different frequencies, f_i, in different subbands: $f_i = 1/\hbar\omega_{ci}$, where index $i = 1(2)$ corresponds to the first (second) subband.

At a small quantizing magnetic fields $\omega_{ci}\tau_q < 1$ the main contribution to MISO comes from the fundamental harmonics of DOS oscillations. The DOS of the ith spatial subband, $\nu_i(\epsilon)$, reads [3,20]

$$\frac{\nu_1(\epsilon \geqslant 0)}{\nu_{01}} = 1 - 2\delta_1 \cos(2\pi f_1 \epsilon),$$

$$\frac{\nu_2(\epsilon \geqslant E_g)}{\nu_{02}} = 1 - 2\delta_2 \cos[2\pi f_2(\epsilon - E_g)], \quad (6)$$

where ν_{0i} represents DOS at zero perpendicular magnetic field, $\delta_i = \exp(-\pi/\omega_{ci}\tau_q^{(i)})$ is the Dingle factor and $\tau_q^{(i)}$ is the quantum scattering time in ith subbands. The parameters ν_{0i} describe the DOS in a kT vicinity of the Fermi energy. Within the kT interval, the energy dependence of these parameters in a weakly nonparabolic spectrum of 2D electrons, induced by the in-plane magnetic field, is neglected.

The 2D conductivity σ is obtained from the following relation:

$$\sigma(\mathbf{B}) = \int d\epsilon \, \sigma(\epsilon)\left(-\frac{\partial f_T}{\partial \epsilon}\right) = \langle\sigma(\epsilon)\rangle. \quad (7)$$

The integral is an average of the conductivity $\sigma(\epsilon)$ taken essentially for energies ϵ inside the temperature interval kT near Fermi energy, where $f_T(\epsilon)$ is the electron distribution function at a temperature T [2,3]. The brackets represent this integral below. We consider the regime of high temperatures: $f_i kT \gg 1$. In this regime, SdH oscillations are suppressed but MISO survive.

The conductivity $\sigma(\epsilon)$ is proportional to square of the total density of states: $\sigma(\epsilon) \sim (\nu_1(\epsilon) + \nu_2(\epsilon))^2$ [20,30]. This relation yields the following term leading to MISO at small

quantizing magnetic fields [13,15]:

$$\sigma_{\text{MISO}}(\epsilon) = \sigma_D^{(12)}\tilde{\nu}_1(\epsilon)\tilde{\nu}_2(\epsilon), \quad (8)$$

where $\tilde{\nu}_i(\epsilon) = \nu_i(\epsilon)/\nu_{0i}$ are the normalized density of states in each spatial subband. The parameter $\sigma_D^{(12)}(B_\perp)$ is Drude-like conductivity, accounting for inter-subband scattering [13,15].

A substitution of Eqs. (8) and (6) into Eq. (7) yields the following expression for the MISO of conductivity:

$$\sigma_{\text{MISO}}(\mathbf{B}) = 4\sigma_D^{(12)}\delta_1\delta_2\langle\cos(2\pi f_1\epsilon)\cos[2\pi f_2(\epsilon - E_g)]\rangle. \quad (9)$$

An energy integration (see details in Appendix B) yields the final result,

$$\sigma_{\text{MISO}}(\mathbf{B}) = 2\sigma_D^{(12)}\delta_1\delta_2\frac{X}{\sinh(X)}\cos(2\pi f_2 E_g + 2\pi\delta f\epsilon_F), \quad (10)$$

where parameter $X = 2\pi^2 kT\delta f$ and $\delta f = f_1 - f_2$.

The obtained expression reproduces the results for disentangled subbands at $B_\parallel = 0$ T [13,15]. Indeed, at $B_\parallel = 0$ T, the difference frequency $\delta f = 0$ and the temperature damping factor $A_{\text{MISO}}(T) = X/\sinh(X) = 1$. The MISO maxima correspond to the condition $f_2 E_g = j$, where j is a positive integer, which is equivalent to Eq. (1) since $f_2 = f_1 = 1/\hbar\omega_c$ and $E_g = \Delta_{12}$ at $B_\parallel = 0$ T. Finally, the MISO magnitude is proportional to the product of two Dingle factors δ_1 and δ_2 [13,15].

For entangled subbands $\delta f > 0$ and the temperature damping factor $A_{\text{MISO}}(T) = X/\sinh(X)$ decreases the MISO amplitude. This temperature decrease becomes exponential for $X > 1$ since $\sinh(X) \sim \exp(X)$ for $X > 1$. The parameter X is proportional to the temperature and the difference frequency $\delta f = f_1 - f_2$. At small in-plane magnetic fields, $B_\parallel$, the difference frequency is proportional to $B_\parallel^2$. This is shown in the inset to Fig. 5 since $\delta f = f(m_{c1} - m_{c2})/m_0$ and $(m_{c1} - m_{c2})/m_0 \approx \chi B_\parallel^2$ at small $B_\parallel$, where χ is a constant. Thus, at small in-plane magnetic fields the parameter $X = 2\pi^2 kTf\chi B_\parallel^2 = [2\pi^2 km_0/(e\hbar)]\chi\tan^2(\theta)TB_\perp$ is proportional to T and $B_\perp$. At larger $B_\parallel$, the mass divergence becomes weaker than $B_\parallel^2$, indicating a presence of high order terms of $B_\parallel^2$. Within the order of $B_\parallel^6$ the parameter X reads

$$X = \frac{2\pi^2 km_0}{e\hbar}\chi(1 - \xi B_\parallel^2 + \eta B_\parallel^4)\tan^2(\theta)TB_\perp, \quad (11)$$

where χ, ξ and η are constants. In Appendix A, the constants $\chi = 1.12 \times 10^{-5}[d(\text{nm})]^2$ and $\xi = 1.91 \times 10^{-5}[d(\text{nm})]^2$ are computed analytically for the magnetically entangled subbands. Below we use the relation Eq. (11) to compare experiments with the expression Eq. (10).

In many respects, the MISO temperature damping factor $A_{\text{MISO}}(T)$ is similar the one for SdH oscillations, $A_{\text{SdH}}(T) = X_{\text{SdH}}/\sinh(X_{\text{SdH}})$, where $X_{\text{SdH}} = 2\pi^2 kT/(\hbar\omega_{ci})$ [1]. The main difference is that the factor A_{MISO} depends on the difference frequency δf whereas the A_{SdH} depends on the frequency $f_i = 1/\hbar\omega_{ci}$. For parabolic subbands with the same masses, $\delta f = 0$ and the MISO damping factor $A_{\text{MISO}} = 1$ is irrelevant. The MISO damping factor is important for nonparabolic spectra or parabolic spectra with different cyclotron masses in two subbands.
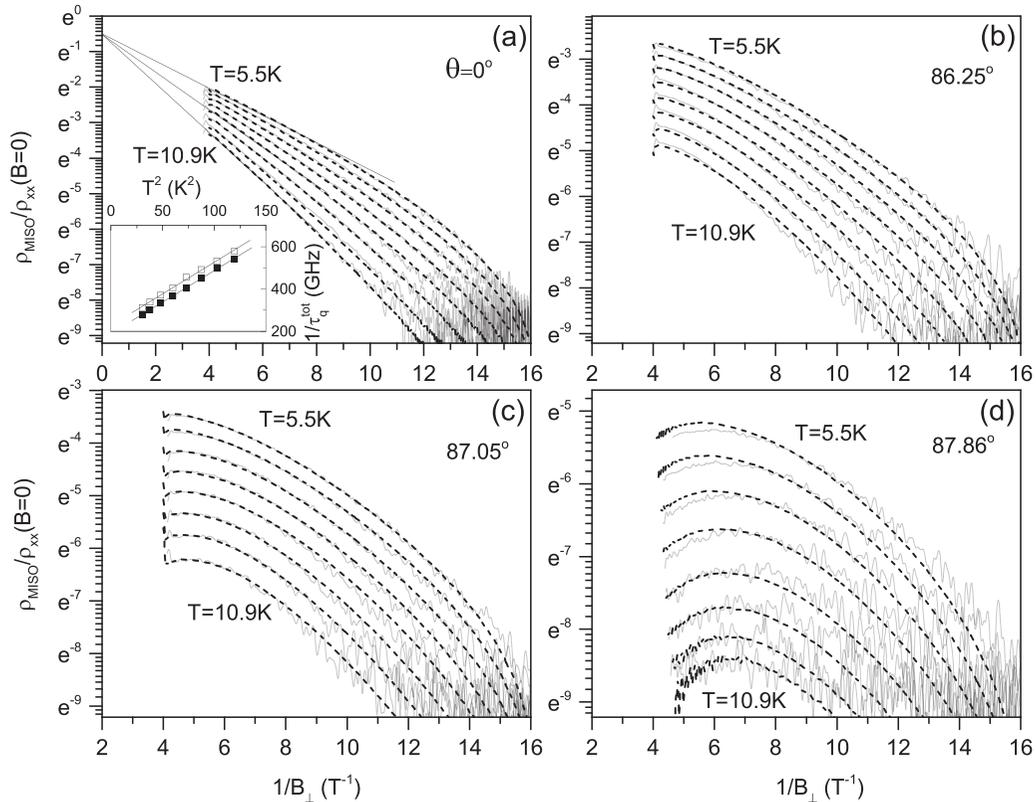
FIG. 7. Dependence of normalized MISO amplitude $\rho_{\mathrm{MISO}}/\rho_{xx}(0)$ on reciprocal magnetic field, $1/B_\perp$, at different temperatures from top to bottom $T = 5.5, 6.14, 6.93, 7.74, 8.54, 9.34, 10.13,$ and 10.93 K and at angles as labeled. Solid lines represent experimental data. Dashed lines are numerical computations of MISO magnitude multiplied with normalizing function $F_N(B_\perp) = 0.55\cos(0.096/B_\perp)$. (a) The numerical computations use quantum scattering times $\tau_q^{(1)} = \tau_q^{(2)}$ as fitting parameters to match with the experiment at different temperatures. In the inset, filled symbols present the obtained total quantum scattering rate: $1/\tau_q^{\mathrm{tot}} = 2/\tau_q^{(1)}$. Open symbols present the rate determined from slopes of the thin straight lines shown in (a); (b)–(d) determined in (a) rates $1/\tau_q^{\mathrm{tot}}$ are used to compute MISO magnitude. The computed dependencies are shifted vertically to match with experiment, using normalizing factor $K(T)$. $d = 26$ nm. Sample S1.

V. TEMPERATURE DEPENDENCE OF MISO IN TILTED MAGNETIC FIELD

In this section, we compare the described model above and numerical computations of MISOs with experiment. We start with the comparison between the numerical estimations and experiment.

Figure 7 presents dependence of MISO amplitude on reciprocal magnetic field, $1/B_\perp$, measured at different temperatures between 5.5 K and 10.9 K. Figures 7(a)–7(d) show the dependencies taken at different angles θ between the normal to 2D layer and the direction of the magnetic field **B**. The dashed lines present results of numerical computations of MISO magnitude.

Figure 7(a) presents the dependencies taken at $\theta = 0^0$. At this angle the entanglement between subbands is absent and $A_{\mathrm{MISO}} = 1$. The MISO magnitude decreases strongly with the reciprocal magnetic field, $1/B_\perp$. This decrease is due to the exponential decrease of Dingle factors δ_i with $1/B_\perp$: $\delta_i = \exp(-\pi/\omega_{ci}\tau_q^{(i)})$. In accordance with Eq. (10), the MISO magnitude is proportional to the product of the Dingle factors. For disentangled subbands, the cyclotron frequencies ω_{c1} and ω_{c2} are the same since $m_{c1} = m_{c2} = m_0$. Thus, the dependencies of the MISO amplitude on $1/B_\perp$, plotted in semilog scale, should be straight lines with the slope proportional to the sum

of quantum scattering rates in two subbands: $1/\tau_q^{(1)} + 1/\tau_q^{(2)}$. In Fig. 7(a), thin solid straight lines present the linear approximation of the measured dependencies. At higher temperature, the slope of the lines becomes larger, indicating an increase of the quantum scattering rate with the temperature increase. In the inset to Fig. 7(a), open symbols presents the temperature dependence of total quantum scattering rate $1/\tau_q^{\mathrm{tot}} = 1/\tau_q^{(1)} + 1/\tau_q^{(2)}$, extracted from these slopes.

A noticeable feature of the linear approximation is the convergence of the straight lines to the single point at $1/B_\perp = 0$ T. This feature follows from Eq. (10) since $\delta_1\delta_2 \to 1$ and, thus, becomes temperature independent at $1/B_\perp \to 0$. Another noticeable feature is the apparent deviation of the measured dependencies from the straight lines at $1/B_\perp > 10$ (1/T). The origin of this deviation is under investigation and is not the focus of this paper. We have found that a normalization of Eq. (10) by a temperature-independent function $F_N(B_\perp)$ leads to a good agreement between experiment and the model.

In Fig. 7(a), the dashed lines present results of the numerical evaluation of the MISO magnitude. For each temperature, the MISO magnitude is evaluated numerically with only one fitting parameter—the total quantum scattering rate $1/\tau_q^{\mathrm{tot}}$. The computed dependence is multiplied by the normalizing function $F_N(B_\perp) = 0.55\cos(0.096/B_\perp)$, which bends down

the linear dependence at $1/B_\perp > 10$, providing good agreement with the experiment. Obtained via this procedure, the total scattering rate is shown by filled symbols in the inset to the figure. This scattering rate is found to be slightly lower than the one obtained via the first procedure (open symbols). Both dependencies essentially demonstrate the same variations of the quantum scattering rate with the temperature, $\delta(1/\tau_q^{\rm tot}) \sim T^2$, indicating the dominant contribution of the electron-electron scattering to the quantum electron lifetime [8,9,19].

For entangled subbands, the cyclotron frequencies ω_{c1} and ω_{c2} are different since $m_{c1} > m_{c2}$. The difference leads to variations of the product of Dingle factors with the in-plane magnetic field in Eq. (10). Both numerical and analytical investigations of these variations demonstrates weak (within a few percent) corrections to MISO magnitude in the studied range of parameters. At $\tau_q^{(1)} = \tau_q^{(2)}$, these corrections are absent. Below we neglect these corrections and use $\tau_q^{(1)} = \tau_q^{(2)}$.

Figure 7(b) presents the magnetic field dependence of the MISO magnitude at $\theta = 86.25°$. At this angle, the magnetic entanglement between two subbands leads to modifications of the MISO magnitude. Indeed, at $1/B_\perp \approx 5$ (1/T) and $T = 5.5$ K, the relative MISO magnitude is 0.058, which is considerably smaller the one shown in Fig. 7(a): 0.094. At higher temperature $T = 10.9$ K, the ratio between these two magnitudes becomes even smaller: 0.37. The numerical evaluations demonstrate the decrease of the MISO magnitude with the magnetic field tilt and temperature and mostly capture the changes in the dependence shape. To better compare variations of the shape of the dependencies, the overall magnitude of the numerical MISO is multiplied by a factor of $K(T)$, which is shown in the inset to Fig. 9. In Figs. 7(b)–7(d), the factor K moves the computed dependencies vertically providing a better overlap with the experiment.

Figures 7(c) and 7(d) present the magnetic field dependence of the MISO magnitude at $\theta = 87.05°$ and $\theta = 87.86°$. At larger tilts, the entanglement between subbands becomes stronger, leading to stronger suppression of the MISO magnitude. The numerical computations continue to demonstrate good correlations with the shape of the magnetic field dependencies at different temperatures. These dependencies are not only quantitatively but qualitatively different from the ones shown in Fig. 7(a) for the disentangled subbands. In particular, the convergence of the responses at $1/B_\perp \to 0$, which is apparent in Fig. 7(a), disappears in Figs. 7(c) and 7(d). Another noticeable feature is a consistent increase of variations of the normalizing coefficient K with the temperature and the tilt, which is shown in the inset to Fig. 9. This MISO property will be discussed later.

All numerical dependencies, shown in Figs. 7(b)–7(d), are obtained at fixed $d = 26$ nm, providing the best agreement with the shapes of experimental dependencies. The quantum scattering rates are determined from the response of disentangled subbands shown in Fig. 7(a). Thus, in Figs. 7(b)–7(d), the only variable fitting parameter is the normalizing factor K, which moves the dependencies vertically but does not change their shape. Thus, as for the functional dependence presented in Figs. 7(b)–7(d), comparison between experiment and the model uses only one fitting parameter—the width of the quantum well d. The obtained width $d = 26$ nm coincides with
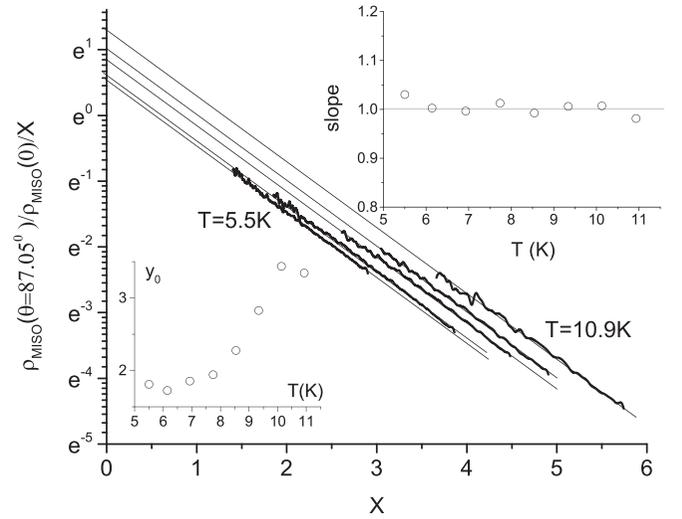
FIG. 8. Dependence of ratio of MISO magnitude at $\theta = 87.05°$ to the one at $\theta = 0°$, normalized by X, on parameter X at different temperatures T: 5.5, 7.74, 8.54, 9.34, and 10.9 K. The parameter X is computed from Eq. (11), using $\chi = 1.12 \times 10^{-5}[d(\rm nm)]^2$, $\xi = 1.91 \times 10^{-5}[d(\rm nm)]^2$, (see Appendix A), and $\eta = 4 \times 10^{-10}[d(\rm nm)]^4$. Thin straight lines present linear dependencies with a unity slope, expected from Eq. (10). Upper inset presents temperature variations of slope magnitude, obtained from linear fit of the normalized ratio. Lower inset presents temperature evolution of the intersect y_0 of the linear fit with y axis.

the actual width of the studied 2D layer. Thus, the presented model captures the variations of the shape of the dependency of MISO on $1/B_\perp$.

Presented in Fig. 7, comparison with the numerical MISO is done under assumptions that the quantum scattering rates $1/\tau_q^{(i)}$ and the Drude-like conductivity $\sigma_D^{(12)}$ do not vary with the entanglement between subbands. The obtained agreement supports these assumptions, which we follow below.

To reveal the temperature damping factor $A_{\rm MISO}(X) = X/\sinh(X)$, we compare our experimental data with the analytical expression Eq. (10) containing this factor. There are other factors (δ_i, $\sigma_D^{(12)}$) entering the expression. The presented comparison above with the numerical MISO as well as analytical considerations indicate that the product of these factors vary very weakly with the entanglement between subbands. Below we neglect these variations. To remove effects of these factors in the comparison between Eq. (10) and experiment, we divide each dependence in Figs. 7(b)–7(d) (entangled subbands) by the dependence from Fig. 7(a) (disentangled subbands) taken at the same temperature T. This ratio $R_{\rm exp} = \rho_{\rm MISO}(\theta)/\rho_{\rm MISO}(0)$ is compared with the one obtained from Eq. (10). In accordance with Eq. (10) at $\tau_q^{(1)} = \tau_q^{(2)}$, the ratio of the MISO magnitudes $R_{\rm mod} = X/\sinh(X)$ and depends only on the parameter X. Thus, plotted versus X, the ratio $R_{\rm exp}(X)$ should follow $A_{\rm MISO}(X) = X/\sinh(X)$. To facilitate the comparison at $X > 1$, both ratios are divided by X, yielding $R_{\rm mod}/X \approx 2\exp(-X)$ at $X > 1$. At large X $\ln(R/X)$ vs X is, thus, a straight line with a unity slope intersecting y axis at $y_0 = 2$.

Figure 8 presents the dependence of the ratio $R_{\rm exp}/X = \rho_{\rm MISO}(\theta)/\rho_{\rm MISO}(0)/X$ on parameter X for data at
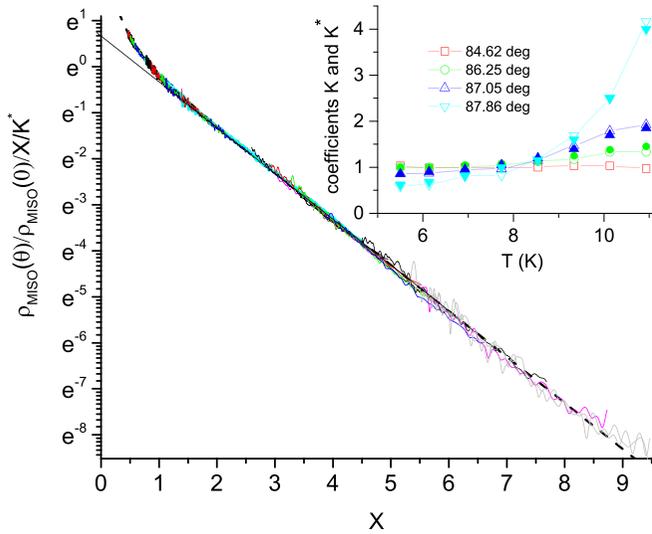
FIG. 9. Dependence of the ratio R of MISO magnitude obtained at angle θ to the one at $\theta = 86.25^{\circ}$ normalized by X and K^*: $R^* = R/X/K^*$ on parameter X at different temperatures T: 5.5, 6.14, 6.93, 7.74, 8.54, 9.34, 10.13, and 10.9 K and different angles $\theta = $ 84.62, 86.25, 87.05, and 87.86° (see text for detail). The parameter X is computed from Eq. (11), using $\chi = 1.12 \times 10^{-5}[d(\text{nm})]^2$, $\xi = 1.91 \times 10^{-5}[d(\text{nm})]^2$, which are evaluated in Appendix A, and $\eta = 4 \times 10^{-10}[d(\text{nm})]^4$ at $d = 26$ nm. Dashed line presents the dependence $1/\sinh(X)$ expected from Eq. (10). Thin straight line presents the linear dependence R/X vs X with a unity slope and intersect $y_0 = 2$, expected from Eq. (10) at $X > 1$. The inset presents temperature dependence of normalizing coefficients K(filled symbols) and K^*(open symbols) at different angles as labeled.

$\theta = 87.05^{\circ}$. The parameter X is evaluated from Eq. (11), using parameters $\chi = 1.12 \times 10^{-5}[d(\text{nm})]^2$ and $\xi = 1.91 \times 10^{-5}[d(\text{nm})]^2$, computed in Appendix A and parameter $\eta = \eta_0[d(\text{nm})]^4$, where η_0 is a fitting parameter. At $d = 26$ nm for all temperatures, the experimental dependencies $\ln(R/X)$ vs X follow the straight lines with unity slope. Some of the straight lines and the dependencies are shown in Fig. 8. The upper inset to Fig. 8 demonstrates the magnitude of slopes obtained by a linear fit of the data. The slope magnitudes fluctuate around the expected value 1.

At $T = 5.5$ K, the intersect of the corresponding straight line with the y axis yields $y_0 \approx 1.72$. This value is slightly below the expected value 2. With an increase of temperature, the intersect y_0 increases. The lower inset presents the increase of the intersect y_0 with the temperature obtained from the linear fit of the data. Thus, similar to the comparison with the numerical MISO, shown in Fig. 7, the comparison in Fig. 8 advocates for an additional factor $K^*(T, \theta)$ controlling the MISO magnitude.

At different temperatures and angles, the normalizing factor K^* is determined by the best overlap of experimental data with the expected dependence $1/\sinh(X)$. To cancel effects related to this factor, the experimental data $R_{\text{exp}} = \rho_{\text{MISO}}(\theta)/\rho_{\text{MISO}}(0)$ is divided by $K^*(T, \theta)$. This procedure leads to a collapse of experimental dependencies on the single curve $1/\sinh(X)$, shown in Fig. 9.

Figure 9 presents the dependence of the normalized ratio $R^* = \rho_{\text{MISO}}(\theta)/\rho_{\text{MISO}}(0)/X/K^*$ on the parameter X for different temperatures and angles. The figure shows that for a broad range of temperatures and subband entanglement, the normalized MISO magnitude, R^*, depends on the single parameter X, demonstrating good agreement with the modified MISO temperature damping factor $A_{\text{MISO}}/X = 1/\sinh(X)$, shown by the dashed line in the figure. Thus, both comparisons, which are presented in Figs. 7–9, indicate that variations of MISO magnitude with the reciprocal magnetic field $1/B_\perp$, temperature T, angles θ agree with the model and are controlled by MISO temperature damping factor $A_{\text{MISO}} = X/\sinh(X)$.

Both comparisons also indicate that there is another controlling factor $K^*(\theta, T) \approx K(\theta, T)$, which is beyond the presented model. The inset to Fig. 9 shows temperature dependencies of normalizing coefficients K (filled symbols) and K^* (open symbols), obtained by different fitting procedures. Both procedures indicate the same temperature increase of both factors at a given angle. The data shows that the temperature variations of parameters K and K^* are larger at larger θ.

At large angles $\theta = 87.05^{\circ}$ and $\theta = 87.86^{\circ}$, the unity slope of the dependencies $R^*(X)$ is observed for all temperatures. However at smaller angles ($\theta = 84.62^{\circ}$ and $\theta = 86.25^{\circ}$) and high temperatures ($T > 9$ K), the dependencies $R^*(X)$ demonstrate slopes with magnitudes which are distinctly smaller than the unity. These dependencies are not shown in Fig. 9. The presence of these deviations suggests a transitional function $F_{\text{tr}}(\delta f, \theta, T)$ between regimes of a weak and strong subband entanglement with a property $F_{\text{tr}}(\delta f, \theta, T) \rightarrow K^*(\theta, T)$ at a large X. The transitional function has not been investigated in this study. At large angles θ and temperatures (large X), where the normalizing coefficient K^* and the function $F_{\text{tr}}(\delta f, \theta, T)$ are measurable, the access to small X requires a very small $B_\perp$ [see Eq. (11)]. At this small $B_\perp$, the Dingle factors strongly suppress the MISO amplitude making the amplitude measurements not accurate. Measurements at smaller angles indicate the presence of the transitional function. However, the magnitude of this function is small, making an analysis of the function to be not informative.

A. Effects of electron-electron interaction on MISO

Both Fig. 8 and the inset to Fig. 9 demonstrate an increase of the deviation between the experiment and model with the temperature increase. The increase of the deviation correlates with the increase of the temperature dependent contribution to the electron lifetime. Indeed, the inset to Fig. 7(a) shows that at $T = 10.9$ K the contribution of electron-electron scattering to the quantum scattering rate is about four times larger than at $T = 5.5$ K and becomes dominant. This correlation suggests that effects of electron-electron interaction or Fermi-liquid effects may play an important role, leading to the deviation between Eq. (10) and experiment. Indeed, although ignored in the presented model, such effects are important for quantum oscillations, resulting in a renormalization of the electron mass and g factor—the effects, which have been intensively investigated both theoretically and experimentally for several decades [3].

Effects of the electron-electron interactions on the quantum scattering time, controlling the magnitude of quantum

oscillations, are less frequently studied. Existing theory predicts that the amplitude of the fundamental harmonic of SdH oscillations is resilient to the temperature variations of the quantum scattering time, induced by the electron-electron interaction [31,32]. In other words, the quantum scattering time, entering the Dingle factor for the fundamental harmonic of SdH oscillations, is a temperature-independent parameter. This can be considered as a result of a modification of the electron lifetime by the electron-electron interaction. The modification leads to contributions, enhancing the SdH amplitude and compensating the temperature-dependent part of the quantum scattering rate in the Dingle factor. In contrast the quantum scattering rate, entering the Dingle factor for the MISO amplitude, is a temperature-dependent property, as shown in the inset to Fig. 7(a).

To the best of our knowledge, Fermi liquid effects related to MISOs in magnetically entangled subbands have not been investigated. Assuming a similarity of the Fermi liquid contributions to the magnitude of SdH oscillations and MISOs in entangled subbands, one should expect a relative increase of the MISO magnitude, which may explain the increase of factors K and K^* with the temperature. The resilience of SdH amplitude to the electron-electron interactions can be obtained via an account of the interaction-induced dependence of the electron-electron scattering rate on the energy ϵ [33]. The electron-electron collision rate for an electron at energy ϵ counted from the Fermi energy ϵ_F is

$$\frac{1}{\tau_{ee}(\epsilon, T)} = \frac{\epsilon^2 + \pi^2(kT)^2}{4\pi\hbar\epsilon_F} \ln\frac{q_s v_F}{\max(kT, \hbar\omega_c(\omega_c\tau_{\mathrm{tr}})^{1/2})}, \tag{12}$$

where v_F is Fermi velocity, τ_{tr} is transport scattering time, and $q_s = 2\pi e^2 \nu$ is inversion screening length [30,33].

The energy dependence of the electron scattering rate makes the Dingle factors δ_i be energy dependent parameters,

$$\delta_i(\epsilon, T) = \exp\left(-\frac{\tau_{im}^{-1} + \tau_{ee}^{-1}(\epsilon, T)}{\omega_{ci}/\pi}\right), \tag{13}$$

where τ_{im} is quantum scattering time due to impurity scattering. The time τ_{im} does not depend on the temperature while the electron-electron scattering time τ_{ee} is temperature dependent. The time τ_{ee} provides the T^2 contribution to the quantum scattering rate shown in the inset to Fig. 7(a) for the disentangled subbands.

The energy dependence of the Dingle factors δ_i is not accounted for in the above-presented analysis. The effect of the energy dependence of the $e - e$ scattering rate on the relative MISO magnitude: $\rho_{\mathrm{MISO}}(\theta)/\rho_{\mathrm{MISO}}(0^\circ) = \sigma_{\mathrm{MISO}}(\theta)/\sigma_{\mathrm{MISO}}(0^\circ)$ is evaluated below. Substitution of the relations Eqs. (8), (6), and (13) into Eq. (7) leads to the following expression for the relative MISO magnitude:

$$\frac{\rho_{\mathrm{MISO}}(\theta)}{\rho_{\mathrm{MISO}}(0^0)} = \frac{\langle \exp\left(-\epsilon^2/\epsilon_0^2\right)\cos(2\pi\delta f\epsilon)\rangle}{\langle \exp\left(-\epsilon^2/\epsilon_0^2\right)\rangle}, \tag{14}$$

where $\epsilon_0 = (2\epsilon_F^*\hbar\omega_c)^{1/2}$. In the estimation, a possible difference in the $e - e$ scattering rate in two subbands and the temperature/magnetic field dependencies of the logarithmic factor in Eq. (12) are ignored. As a result, in Eq. (14) the only fitting parameter is $\epsilon_F^* \sim \epsilon_F^{(i)}/\ln(q_s v_F^{(i)}/\max(kT, \hbar\omega_c(\omega_c)^{1/2}))$.
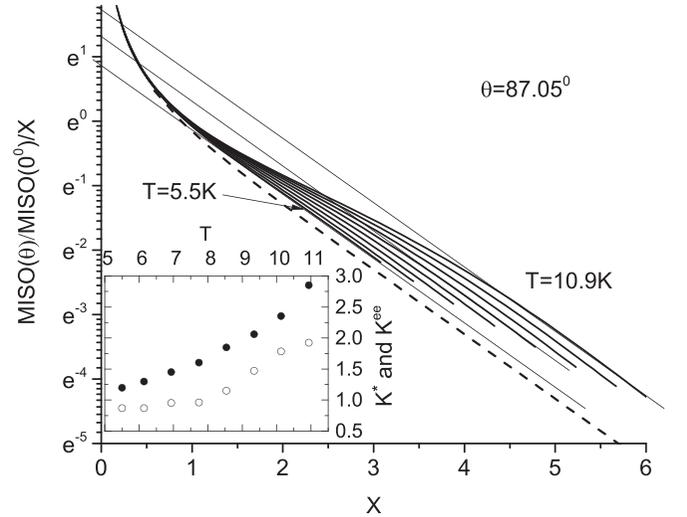
FIG. 10. Dependence of ratio of MISO magnitude at $\theta = 87.05^\circ$ to the one at $\theta = 0^\circ$, normalized by X on parameter X. The dependence is computed at $\epsilon_F^* = 8$ meV and different temperatures from bottom to top $T = 5.5, 6.14, 6.93, 7.74, 8.54, 9.34, 10.13$, and 10.9K using Eq. (14). The parameter X is computed from Eq. (11), using $\chi = 1.12 \times 10^{-5}[d(\mathrm{nm})]^2$, $\xi = 1.91 \times 10^{-5}[d(\mathrm{nm})]^2$, obtained in Appendix A, and $\eta = 4 \times 10^{-10}[d(\mathrm{nm})]^4$. Thin straight lines present linear dependencies with a unity slope. Dashed line displays free electron response $1/\sinh(X)$. The inset shows temperature evolution of factors K^* and K^{ee}, characterizing maximal deviation of the experimental and model data from the free electron response.

Figure 10 demonstrates the dependence of normalized relative MISO magnitude, $\rho_{\mathrm{MISO}}(\theta)/\rho_{\mathrm{MISO}}(0^0)/X$ on parameter X obtained from Eq. (14) at angle $\theta = 87.05^0$, temperatures $T = 5.5, 6.14, 6.93, 7.74, 8.54, 9.34, 10.13$, and 10.9K and $\epsilon_F^* = 8$ meV. The angle and temperatures correspond to the experimental dependencies of the normalized relative MISO magnitude presented in Fig. 8. In Fig. 10, the dashed line shows the dependence $1/\sinh(X)$ for free 2D electrons computed at $\epsilon_0 \to \infty$. The obtained behavior suggests that the relative MISO magnitude can be presented as a product of $X/\sinh(X)$ and a finite function $F_{\mathrm{tr}}(X, \theta, T)$:

$$\frac{\rho_{\mathrm{MISO}}(\theta)}{\rho_{\mathrm{MISO}}(0^0)} = F_{\mathrm{tr}}(X, \theta, T)\frac{X}{\sinh(X)}. \tag{15}$$

Below we investigate properties of the function $F_{\mathrm{tr}}(X, \theta, T)$. In Fig. 10, at small $X < 1$ the dependencies converge for all temperatures. This is related to the reduction of the difference frequency: $\delta f \to 0$ at $X \to 0$ since δf is proportional to X. At $\delta f \to 0$ in Eq. (14) the cosine function tends to 1 and the ratio of the two integrals approaches unity. Thus, at $X \to 0$ the function $F_{\mathrm{tr}}(X, \theta, T) \to 1$ since $X/\sinh(X) \to 1$.

At large $X \to \infty$ but a finite temperature, the function $F_{\mathrm{tr}}(X, \theta, T)$ also tends to unity. To understand this property, we note that in accordance with Eq. (11) a large X corresponds to a large $B_\perp$ and, thus, to large $\hbar\omega_c$ and ϵ_0. At $\epsilon_0 \gg kT$ in Eq. (14), the Gaussian functions can be neglected that leads to the free electron result Eq. (10).

At an intermediate X, the function $F_{\mathrm{tr}}(X, \theta, T)$ deviates from unity and reaches a maximum. The increase of the

function $F_{tr}(X, \theta, T)$ from unity is a result of the electron-electron interaction and thus is a Fermi liquid effect. The electron-electron interaction leads to a decrease of the quantum lifetime of quasiparticles with the energy ϵ away from the Fermi energy [31,32]. Equations (12) and (13) take into account this lifetime decrease and yields in Eq. (14) the Gaussian $\exp(-\epsilon^2/\epsilon_0^2)$, which enhances the MISO amplitude. Mathematically, the effect is due to a reduction of the range of the energy integration in Eq. (14) from $(-kT, kT)$, settled by the distribution function f_T for free electrons, to a smaller range, which for the interacting electrons is additionally affected by the range narrowing factor $\exp(-\epsilon^2/\epsilon_0^2)$. The energy averaging of the oscillating content $[\cos(2\pi\delta f \epsilon)]$ in narrower energy intervals leads to a suppression of the averaging and results in a larger value of the integral and, thus, the function $F_{tr}(X, \theta, T)$ [33].

In the experimentally studied range of parameters, the maximum of the function $F_{tr}(X, \theta, T)$ appears to be quite flat and can be approximated by a straight horizontal line, which acquires a unity slope in Fig. 10. This property agrees with the experiment. Three of these lines are shown in Fig. 10. A coefficient $K^{ee}(T) \approx \max[F_{tr}(X, T)]$ characterizes the vertical displacement of these lines from the free electron response $1/\sinh(X)$ (dashed line). Figure 10 demonstrates that the coefficient $K^{ee}(T)$ increases with the temperature. This behavior is also in agreement with the experiment shown in Fig. 8.

The inset to Fig. 10 demonstrates a comparison between coefficient K^*, obtained from experimental data presented in Fig. 8 and coefficient K^{ee}, obtained from the model data presented in Fig. 10. At $\epsilon_F^* = 8$ meV, both coefficients K^*, K^{ee} and variations of these coefficients with the temperature are close to each other. Furthermore, an evaluation of the temperature dependence of the quantum scattering rate, using the temperature-dependent part of Eq. (12), yields $\tau_q^{-1}(T) - \tau_q^{-1}(0\,\text{K}) = \tau_{ee}^{-1}(\epsilon = 0) = \pi(kT)^2/(4\hbar\epsilon_F^*) \approx 1.2(\text{GHz})T^2$. This value is close to the inelastic scattering rate obtained in the experiment at $\theta = 0^o$ and shown in the inset to Fig. 7(a): $\tau_q^{-1}(T) - \tau_q^{-1}(0\,\text{K}) \approx 1.5\,(\text{GHz})\,T^2$. Thus, the account of the electron-electron interaction improves the agreement between the experiment and model, revealing the interaction induced enhancement of MISO amplitude.

VI. SUMMARY

MISOs of highly mobile 2D electrons in symmetric GaAs quantum wells with two populated subbands are studied at different temperatures and at different angles θ between magnetic field **B** and the normal to 2D layer. The experiments indicate that the MISO magnitude decreases strongly with the temperature. For angles $\theta < 80^o$, the MISO reduction is related to the increase of the quantum scattering rate due to the enhancement of electron-electron scattering at high temperatures. For angles $\theta > 80^o$, a different regime of strong MISO damping with the temperature is identified.

Proposed model considers the magnetic entanglement between subbands, which is induced by in-plane magnetic field, as the main reason for the new temperature damping. The entanglement changes the electron spectrum and leads to

different cyclotron masses in two subbands. As a result, the density of states exhibits beating with the difference frequency δf proportional to the mass difference. The model yields universal temperature damping factor $A_{MISO} = X/\sinh(X)$, where $X = 2\pi^2 kT\delta f$.

A comparison of the model with the experiment demonstrates the presence of the factor A_{MISO} but indicates an additional factor $K(T)$, which is beyond the free electron model. The factor K leads to an effective enhancement of the MISO amplitude at high temperatures. An account of the electron-electron interaction explains the enhancement of the MISO amplitude and reveals the Fermi liquid origin of the factor K.

APPENDIX A: COMPUTATION OF DIFFERENCE FREQUENCY

In this Appendix, the spectrum of the entangled subbands is computed at $\theta = 90^o$. The cyclotron masses, m_{ci} and difference frequency $\delta f \sim (m_{c1} - m_{c2})$, are evaluated then for the quasiclassical electron motion in a small $B_\perp$. The goal is estimation of the variations of the parameter $X \sim \delta f$ with the magnetic field $B_\parallel$ leading to Eq. (11).

At $B_\perp = 0$ T ($\mathbf{B} = (-B_\parallel, 0, 0)$), the Hamiltonian Eq. (2) is presented in the following form:

$$H = \frac{\hbar^2 k_x^2}{2m_0} + \frac{\hbar^2(k_y + \frac{eB_\parallel z}{\hbar})^2}{2m_0} + \frac{\hbar^2 k_z^2}{2m_0} + V(z) = H_0 + H_1,$$

$$H_0 = \frac{\hbar^2}{2m_0}(k_x^2 + k_y^2 + k_z^2) + V(z),$$

$$H_1 = \hbar\omega_\parallel k_y z + \frac{1}{2}m_0\omega_\parallel^2 z^2, \tag{A1}$$

where $\omega_\parallel = eB_\parallel/m_0$ is the cyclotron frequency in in-plane magnetic field, $B_\parallel$. At $B_\parallel = 0$ T, the corresponding eigenfunctions $|\mathbf{k}, \xi\rangle$ of the system are plane waves, propagating in $x - y$ plane, and standing waves in the z direction, where wave vector $\mathbf{k}$ describes the lateral motion and $\xi = S, AS$ describes the symmetric (S) and antisymmetric (AS) configurations of the wave function in the z direction (vertical quantization): $|\mathbf{k}, S\rangle = |\mathbf{k}\rangle(2/d)^{1/2}\cos(\pi z/d)$ and $|\mathbf{k}, AS\rangle = |\mathbf{k}\rangle(2/d)^{1/2}\sin(2\pi z/d)$.

Using functions $|\mathbf{k}, \xi\rangle$ as the basis set, one can present the Hamiltonian as a 2×2 matrix:

$$H_{ij} = \epsilon_i^0\delta_{ij} + (1 - \delta_{ij})h_{12},$$

$$\epsilon_i^0 = \frac{\hbar^2}{2m_0}(k_x^2 + k_y^2) + E_i + \frac{1}{2}m\omega_\parallel^2 Z_i^2,$$

$$h_{12} = \hbar\omega_\parallel k_y Z_0, \tag{A2}$$

where δ_{ij} presents 2×2 unit matrix, $Z_0 = 16d/(9\pi^2)$, $Z_1^2 = (1/12 - 1/(2\pi^2))d^2$ and $Z_2^2 = (1/12 - 1/(8\pi^2))d^2$. Indexes $i, j = 1,2$ describes first (1) and second (2) subbands. Energy E_i corresponds to the bottom of i-th subband at $B_\parallel = 0$ T.

At $h_{12} \ll \epsilon_2^0 - \epsilon_1^0$, diagonalization of the Hamiltonian H_{ij} leads to the following spectrum:

$$
\begin{aligned}
\epsilon_i(\mathbf{k}) &\approx \epsilon_i^0(\mathbf{k}) \pm \frac{h_{12}^2}{\epsilon_2^0 - \epsilon_1^0} \left(1 - \frac{h_{12}^2}{\left(\epsilon_2^0 - \epsilon_1^0\right)^2} \right) \\
&\approx \epsilon_i^0(\mathbf{k}) \pm A \frac{\hbar^2 k_y^2}{2m_0} \left(1 - \frac{A}{E_g} \frac{\hbar^2 k_y^2}{2m_0} \right) \\
&= E_i + \frac{\hbar^2 k_x^2}{2m_{xi}} + \frac{\hbar^2 k_y^2}{2m_{yi}} \mp \gamma_0 k_y^4,
\end{aligned}
$$
(A3)

$$
A = \frac{2m_0 Z_0^2}{E_g} \omega_\parallel^2; \quad E_g = \Delta_{12} + \frac{m_0 (Z_2^2 - Z_1^2)}{2} \omega_\parallel^2,
$$

where lower (upper) sign corresponds to the first $(i = 1)$ [second $(i = 2)$] subband, $\gamma_0 = \hbar^4 A^2 / [(2m_0)^2 E_g]$ and $\Delta_{12} = E_2 - E_1$. Equation (A3) indicates that due to the presence of the in-plane magnetic field the spectrum is anisotropic but still parabolic in the lowest order of $B_\parallel$ ($\sim B_\parallel^2$). The parameter A controls the strength of the anisotropy leading to an increase (decrease) of the mass, $m_{y1} = m_0/(1 - A)^{1/2}$ $(m_{y2} = m_0/(1 + A)^{1/2})$ in the y direction for lower (upper) subband. In the x direction, masses do not change: $m_{xi} = m_0$.

For a parabolic spectrum, the cyclotron mass is $m_c = (m_x m_y)^{1/2}$ [2]. To compute the cyclotron masses in the vicinity of Fermi energy ϵ_F for the nonparabolic spectrum we use the relation $m_c = (\hbar^2/2\pi)(\partial S/\partial \epsilon)$, where $S(\epsilon)$ is the area within the contour $\epsilon_i(\mathbf{k}) = \epsilon_F$.[2] For the spectrum Eq. (A3), the result is

$$
m_{c1} = (m_{x1} m_{y1})^{1/2} \left(1 - \frac{3}{4} \frac{m_{y1}^2}{m_0^2} \frac{A^2}{E_g} \epsilon_{F1} \right),
$$

$$
m_{c2} = (m_{x2} m_{y2})^{1/2} \left(1 + \frac{3}{4} \frac{m_{y2}^2}{m_0^2} \frac{A^2}{E_g} \epsilon_{F2} \right), \quad \text{(A4)}
$$

where ϵ_{Fi} is Fermi energy counted from the bottom of ith subband. The result agrees with the numerical computation of the cyclotron masses presented in the inset to Fig. 5:

m_{c1} (m_{c2}) increases (decreases) with the in-plane magnetic field. Furthermore, the sum of the masses stays the same: $m_{c1} + m_{c2} = 2m_0$ within the computed order $B_\parallel^4$.

Within the same order for difference frequency Eq. (A4) yields

$$
\delta f \approx f \left(A - \frac{3}{4} \frac{\epsilon_{F1} + \epsilon_{F2}}{E_g} A^2 \right) \approx f[\chi B_\parallel^2 (1 - \xi B_\parallel^2)],
$$

$$
\chi = \frac{2e^2 Z_0^2}{\Delta_{12} m_0}; \xi = \frac{3}{4} \frac{\epsilon_{F1}^0 + \epsilon_{F2}^0}{\Delta_{12}} \chi + \frac{1}{2} \frac{2e^2 (Z_2^2 - Z_1^2)}{\Delta_{12} m_0}, \quad \text{(A5)}
$$

where ϵ_{Fi}^0 is Fermi energy counted form the bottom of ith subband at zero magnetic field. For the studied system $\epsilon_{F1}^0 = 21.83$ (meV); $\epsilon_{F2}^0 = 6.68$ (meV) and $\Delta_{12} = 15.15$(meV) yield $\chi = 1.12 \times 10^{-5}[d(\text{nm})]^2$ and $\xi = 1.91 \times 10^{-5}[d(\text{nm})]^2$. These results are used to compute the parameter X in Eq. (11) up to terms proportional to $B_\parallel^4$.

APPENDIX B: COMPUTATION OF INTEGRAL IN EQ. (9)

The expression Eq. (9) contains energy integration of a product of two cosine functions. To perform the integration, we represent this product as a sum of two cosines, oscillating at frequencies $f_1 + f_2$ and $\delta f = f_1 - f_2$. An integration of the cosine, oscillating at frequency $f_1 + f_2$, leads to an exponentially small term $\sim \exp(-2\pi^2 (f_1 + f_2)kT)$. Since $f_i kT \gg 1$, this term is neglected.

To perform the integration in the kT vicinity of Fermi energy ϵ_F, we substitute $\epsilon = u + \epsilon_F$. After the substitution the phase of the second cosine, oscillating at frequency δf is a sum of two terms: $\alpha = \pi \delta f u \sim u$ and $\beta = 2\pi (f_2 \Delta_g + \delta f \epsilon_F) = \text{const}$. The cosine can be rewritten using the identity $\cos(\alpha + \beta) = \cos(\alpha)\cos(\beta) - \sin(\alpha)\sin(\beta)$. An integration of the product of two sine functions in the vicinity of the Fermi energy yields zero, since $\sin(\alpha)$ is an odd function of variable u, whereas $\partial f_T(u)/\partial u$ is even function of u. As a result, the integral is proportional to $\langle \cos(2\pi \delta f u) \rangle \cos(2\pi f_2 \Delta_g + 2\pi \delta f \epsilon_F)$. The integration versus u yields $\langle \cos(2\pi \delta f u) \rangle = X/\sinh(X)$, where $X = 2\pi^2 kT \delta f$ [2], leading to Eq. (10).

[1] D. Shoenberg, *Magnetic Oscillations in Metals* (Cambridge University Press, New York, 1984).

[2] J. M. Ziman, *Principles of the Theory of Solids* (Cambridge University Press, Cambridge, UK, 1972).

[3] T. Ando, A. B. Fowler, and F. Stern, Rev. Mod. Phys. B **54**, 437 (1982).

[4] S. D. Sarma and A. Pinczuk, *Perspectives in Quantum Hall Effects*, (Wiley-VCH, Weinheim, 2004).

[5] P. T. Coleridge, Semicond. Sci. Technol. **5**, 961 (1990).

[6] D. R. Leadley, R. Fletcher, R. J. Nicholas, F. Tao, C. T. Foxon, and J. J. Harris, Phys. Rev. B **46**, 12439 (1992).

[7] A. Bykov, D. R. Islamov, A. V. Goran, and A. I. Toropov, JETP Lett. **87**, 477 (2008).

[8] N. C. Mamani, G. M. Gusev, T. E. Lamas, A. K. Bakarov, and O. E. Raichev, Phys. Rev. B **77**, 205327 (2008).

[9] A. V. Goran, A. A. Bykov, A. I. Toropov, and S. A. Vitkalov, Phys. Rev B **80**, 193305 (2009).

[10] A. A. Bykov, A. V. Goran, and S. A. Vitkalov, Phys. Rev. B **81**, 155322 (2010).

[11] L. I. Magarill and A. A. Romanov, Fiz. Tverd. Tela **13**, 993 (1971) [Sov. Phys. Solid State **13**, 828 (1971)].

[12] V. M. Polyanovskii, Fiz. Tekh. Poluprovodn. **22**, 2230 (1988); [Sov. Phys. Semicond. **22**, 1408 (1988)].

[13] M. E. Raikh and T. V. Shahbazyan, Phys. Rev. B **49**, 5531 (1994).

[14] N. S. Averkiev, L. E. Golub, S. A. Tarasenko, and M. Willander, J. Phys.: Condens. Matter **13**, 2517 (2001).

[15] O. E. Raichev, Phys. Rev. B **78**, 125304 (2008).

[16] W. Mayer, S. Vitkalov, and A. A. Bykov, Phys. Rev B **96**, 045436 (2017).

[17] M. G. Vavilov and I. L. Aleiner, Phys. Rev. B **69**, 035303 (2004).

[18] N. C. Mamani, G. M. Gusev, E. C. F. da Silva, O. E. Raichev, A. A. Quivy, and A. K. Bakarov, Phys. Rev. B **80**, 085304 (2009).

[19] S. Dietrich, S. Vitkalov, D. V. Dmitriev, and A. A. Bykov, Phys. Rev. B **85**, 115312 (2012).

[20] W. Mayer, A. Ghazaryan, P. Ghaemi, S. Vitkalov, and A. A. Bykov, Phys. Rev.B **94**, 195312 (2016).

[21] S. Haroche, Rev. Mod. Phys. **85**, 1083 (2013).

[22] J. M. Fink, L. Steffen, P. Studer, L. S. Bishop, M. Baur, R. Bianchetti, D. Bozyigit, C. Lang, S. Filipp, P. J. Leek, and A. Wallraff, Phys. Rev. Lett. **105**, 163601 (2010).

[23] A. Bienfait, J. J. Pla, Y. Kubo, X. Zhou, M. Stern, C. C. Lo, C. D. Weis, T. Schenkel, D. Vion, D. Esteve, J. J. L. Morton and P. Bertet, Nature **531**, 74 (2016).

[24] K. M. Yunusova, D. Konstantinov, H. Bouchiat, and A. D. Chepelianskii, Phys. Rev. Lett. **122**, 176802 (2019).

[25] K.-J. Friedland, R. Hey, H. Kostial, R. Klann, and K. Ploog, Phys. Rev. Lett. **77**, 4616 (1996).

[26] D. V. Dmitriev, I. S. Strygin, A. A. Bykov, S. Dietrich, and S. A. Vitkalov, JETP Lett. **95**, 420 (2012).

[27] J. Kanter, S. Vitkalov, and A. A. Bykov, Phys. Rev. B **97**, 205440 (2018).

[28] M. Sammon, M. A. Zudov, and B. I. Shklovskii, Phys. Rev. Material **2**, 064604 (2018).

[29] T. Akiho and K. Muraki, Phys. Rev. Appl. **15**, 024003 (2021).

[30] I. A. Dmitriev, M. G. Vavilov, I. L. Aleiner, A. D. Mirlin, and D. G. Polyakov, Phys. Rev. B **71**, 115316 (2005).

[31] G. W. Martin, D. L. Maslov, and M. Yu. Reizer, Phys. Rev. B **68**, 241309(R) (2003).

[32] Y. Adamov, I. V. Gornyi, and A. D. Mirlin, Phys. Rev. B **73**, 045426 (2006).

[33] I. A. Dmitriev, M. Khodas, A. D. Mirlin, D. G. Polyakov, and M. G. Vavilov, Phys. Rev. B **80**, 165327 (2009).